Vascular contrast in narrow-band and white light imaging

V. N. Du Le,[1,2,3] Quanzeng Wang,[1] Taylor Gould,[1] Jessica C. Ramella-Roman,[2,4] and T. Joshua Pfefer[1,*]

[1]Center for Devices and Radiological Health, Food and Drug Administration, Silver Spring, Maryland 20993, USA

[2]Department of Biomedical Engineering, Catholic University of America, Washington, DC 20064, USA

[3]Currently at the Department of Medical Physics and Applied Radiation Sciences, McMaster University, Hamilton, Ontario L8S 4L8, Canada

[4]Currently at the Department of Biomedical Engineering and Herbert Wertheim College of Medicine, Florida International University, Miami, Florida 33174, USA

*Corresponding author: joshua.pfefer@fda.hhs.gov

Received 11 September 2013; revised 10 March 2014; accepted 22 April 2014; posted 21 May 2014 (Doc. ID 197454); published 19 June 2014

Narrow-band imaging (NBI) is a spectrally selective reflectance imaging technique that is used clinically for enhancing visualization of superficial vasculature and has shown promise for applications such as early endoscopic detection of gastrointestinal neoplasia. We have studied the effect of vessel geometry and illumination wavelength on vascular contrast using idealized geometries in order to more quantitatively understand NBI and broadband or white light imaging of mucosal tissue. Simulations were performed using a three-dimensional, voxel-based Monte Carlo model incorporating discrete vessels. In all cases, either 415 or 540 nm illumination produced higher contrast than white light, yet white light did not always produce the lowest contrast. White light produced the lowest contrast for small vessels and intermediate contrast for large vessels (diameter $\geq$ 100 μm) at deep regions (vessel depth $\geq$ 200 μm). The results show that 415 nm illuminations provided superior contrast for smaller vessels at shallow depths while 540 nm provided superior contrast for larger vessels in deep regions. Besides 540 nm, our studies also indicate the potential of other wavelengths to achieve high contrast of large vessels at deep regions. Simulation results indicate the importance of three key mechanisms in determining spectral variations in contrast: intravascular hemoglobin (Hb) absorption in the vessel of interest, diffuse Hb absorption from collateral vasculature, and bulk tissue scattering. Measurements of NBI contrast in turbid phantoms incorporating 0.1-mm-diameter hemoglobin-filled capillary tubes indicated good agreement with modeling results. These results provide quantitative insights into light-tissue interactions and the effect of device and tissue properties on NBI performance.

OCIS codes: (170.3660) Light propagation in tissues; (170.3880) Medical and biological imaging.
http://dx.doi.org/10.1364/AO.53.004061

1. Introduction

Mucosal cancers arising in the oral cavity, pharynx, esophagus, and digestive system represent a major public health concern resulting in nearly 140,000 deaths annually in the U.S. [1]. It has been reported that the invasion of tumors into submucosal layers is associated with increased microvessel density and capillary loops that can become dilated and elongated [2]. Histological studies have shown that intratumoral microvessel density increases in proportion to the progression of esophageal Barrett's-associated adenocarcinoma [3,4]. Thus, improved visualization of mucosal vasculature should provide useful information for early detection of mucosal cancer. Recent clinical studies have indicated that, in comparison with conventional white light imag-

1559-128X/14/184061-11$15.00/0

ing, narrow-band imaging (NBI) has the potential to improve detection of mucosal neoplasia in the colon [5,6] and esophagus [7]. In addition, NBI systems associated with magnifying endoscopy have been used to evaluate microvessel features of the esophagus [8] and to distinguish capillary morphology for early detection of oral neoplastic lesions [9], superficial esophageal lesions [10], and gastroesophageal reflux disease [11]. Key advantages of NBI over other optical imaging modalities such as photoacoustic imaging and optical coherence technology include lower cost, simplicity of instrumentation, compatibility with existing endoscope designs, and, perhaps most importantly, the ability to provide wide-field imaging of near-surface tissue features in real time.

The basic theory of NBI is based on hemoglobin (Hb) absorption and wavelength dependent characteristics of tissue optical properties (OPs). Hb has absorption peaks in blue (415 nm) and green (540 nm) regions of the spectrum while mucosal scattering decays monotonically with increasing wavelength [9,12]. Thus, 415 nm illumination can be used to enhance mucosal capillaries in superficial regions while illumination at 540 nm enables improved visualization of vessels in deeper regions. A filter set incorporating center wavelengths of 415, 445, and 500 nm was used in clinical studies by Gono *et al.*, which classified mucosal patterns into three classes with diameters ranging from 10 to 500 μm [13]. Other studies have involved the use of a set of filters with center wavelengths of 415 and 540 nm. NBI systems with this filter set have been used to enhance mucosal capillary patterns under the tongue [14] and to diagnose biliary-tract diseases [15], gastric cancer [16], and lung cancer [17], as well as for *in vivo* studies of colitis [18].

Both single- and dual-band NBI approaches have been studied for cervical cancer detection [19–22]. In conventional colposcopic procedures, white light and single-band NBI near 540 nm are commonly used to detect abnormal features of the cervix [21,22]. However, conventional colposcopy may not provide accurate detection if the changes are minor and at an early stage [20]. An initial study combining dual-wavelength NBI at 415 and 540 nm with conventional colposcopy to improve the identification of small vascular patterns was first proposed by Fujii *et al.* [19]. In addition, the use of 540 nm filters has been applied to laparoscopic surgery by Akbari *et al.*, who showed that vascular visualization could be improved by 100% [23].

While the underlying optical mechanisms of NBI are considered to be well established in the clinical NBI literature [9,12,24], rigorous theoretical analyses of NBI and the effect of tissue and device parameters on its performance have not been performed. In a recently published Letter, we introduced a Monte Carlo (MC) model for evaluating contrast in NBI systems and implemented it to provide initial insights into the differences between illumination at 415 and 540 nm [25]. The model incorporated mucosal tissue layer and vessel-like structures in a three-dimensional (3D), voxel-based approach [26]. Our results indicated that the primary difference in depth selectivity between these wavelengths was not the commonly cited mechanism of differences in scattering but rather differences in Hb absorption. In the current study, we perform a more thorough analysis of NBI, including simulations of white light imaging, an analysis of the effect of changes in illumination wavelength, presentation of fluence data, and investigation of a larger parameter space. Specifically, the current study involved over 1500 simulations covering 51 wavelengths from 400 to 650 nm as well as the original wavelength bands at 415 and 540 nm, for a variety of vessel sizes and depths. Validation of the model was performed via experimental measurements of mucosal tissue-simulating phantoms with a cylindrical inclusion of variable depth.

2. Method

A. Monte Carlo Modeling

The idealized scenario incorporated in our model—cylindrical vessels in homogeneous tissue regions—is analogous to approaches that have been used previously to elucidate light-tissue interactions during laser treatment of Port Wine Stains in skin [27]. Mucosal tissues such as those lining the cervix and esophagus may have two distinct layers—an epithelium with a thickness range of 100–500 μm [28,29] and a mucosal layer approximately 1.5 mm thick [30,31]. Each tissue type in our model has distinct OPs as a function of wavelength–absorption coefficient (μ_a) and reduced scattering coefficient (μ_s'). OPs used for epithelium [32], normal mucosa [33], and blood [34] are shown in Fig. 1. A material grid array composed of cubic voxels measuring 10 μm in each direction was generated to specify the tissue consisting of a 0.1 mm thick epithelium layer, a 0.9 mm thick mucosal layer, and a single discrete cylindrical vessel of varying diameter (D) and depth (Z_V) [25]. D ranged from 20 to 400 μm, corresponding to those found in mucosal tissues [13]. The lateral dimensions of the grid were 3 mm × 3 mm for large vessels ($D \geq 200$ μm) and 1.4 mm × 1.4 mm for small vessels ($D \leq 100$ μm). Z_V was defined as the distance from the top surface of the epithelium to the vessel's top boundary and ranged from 20 to 400 μm. An example of the simulated tissue geometry is shown in Fig. 2.

Simulations involved photons that were launched at normal incidence into the tissue and underwent stochastic propagation and scattering processes based on the weighted-photon Monte Carlo approach and a Henyey–Greenstein phase function. Photons remitted at the tissue surface were subject to a detection restriction based on a numerical aperture (NA) of 0.22, in order to approximate the angular restrictions on light collected by an endoscopic imaging system during clinical use. Each of the

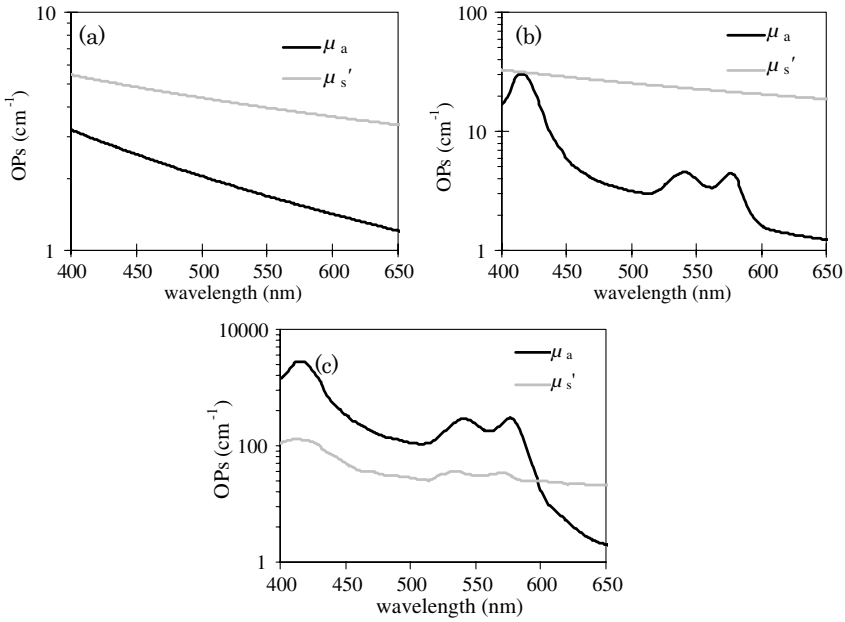

Fig. 1. Absorption coefficient (μ_a) and reduced scattering coefficient (μ_s') of (a) epithelium, (b) mucosa, and (c) oxygenated human blood.

simulations performed in this study included 400 million photons on a supercomputer (110 computing nodes, IBM x3650 M2, 8 CPUs each at 2.67 GHz with 24 GB RAM), requiring approximately 10 h of processor time. The 3D voxel-based MC model of photon propagation is described in further detail elsewhere [26].

B. Contrast Calculation

The primary output of the MC model was a tissue-surface reflectance image distribution [Fig. 3(a)]. In both simulated and experimental images, contrast (C) was quantified using Weber's law as shown in Eq. (1):

$$C = \frac{I_b - I_V}{I_b}, \tag{1}$$

where I_b is the signal intensity in the background region and I_V is intensity in the blood vessel area [Fig. 3(b)]. This method has been applied in previous NBI studies [13,35]. Intensity values represent local reflectance normalized to maximum reflectance intensity; thus I_b, I_v, and C are dimensionless. In each simulated image, the mean intensity distribution in the X direction was determined (140/300 rows for small/large vessels). The background intensity value, I_b, is the mean of 10 adjacent points toward the image edge, and I_v is the mean of five adjacent points in the region of the vessel. In each experimental image, a mean contrast value was calculated for every 10 rows in the image. The mean of five contrast values representing intensity distributions with the least noise was then calculated. In the case where C was less than 10% and it was difficult to distinguish the blood vessel region from the background, C was assigned a zero value. Contrast is a dependent variable that was studied as a function of D, Z_V, OPs, and wavelength.

C. Single- and Multiple-Simulation Approaches

Figure 4 shows the illumination spectra of a conventional white light system and of an NBI system with bandpass filters of 415 ± 15 nm and 540 ± 10 nm [36,37]. In order to reduce the need for multiple MC simulations across specific bandwidths, we investigated the use of a weighted OP, or "single-simulation" method. In this approach, a single set of OPs was determined for an illumination

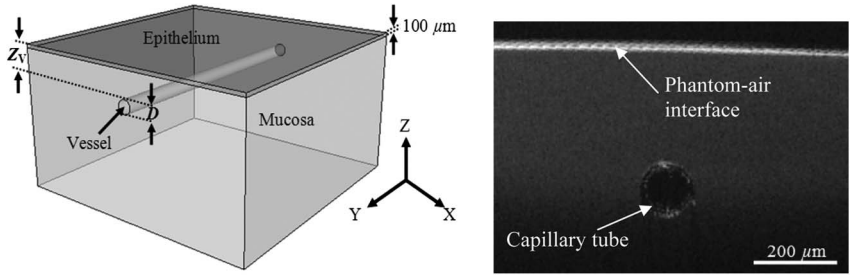

Fig. 2. Simulated tissue geometry (left, where D is vessel diameter and Z_V is vessel depth) and example OCT image of the capillary tube phantom when $D = 100$ μm and $Z_V = 300$ μm (right).

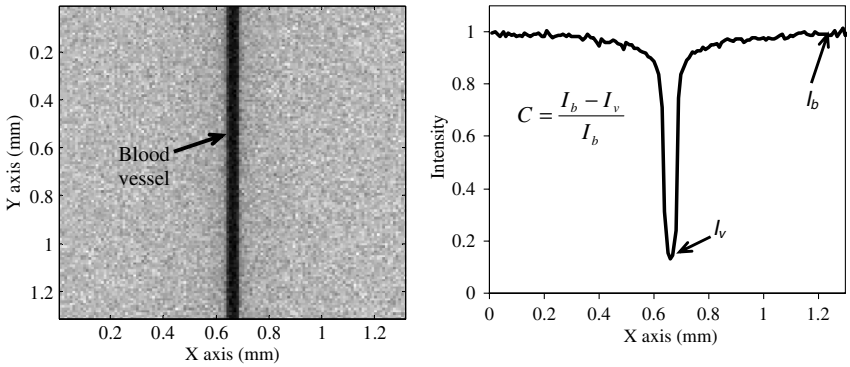

Fig. 3. Simulated reflectance image in X–Y plane (left) and graph of intensity (normalized) as a function of position along the X axis (right), with labels illustrating methodology for calculating vessel contrast.

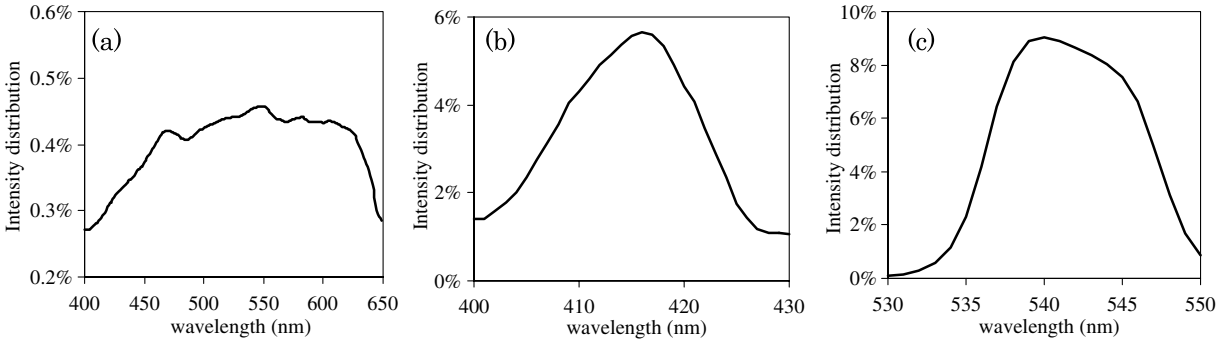

Fig. 4. Illumination spectra of conventional white light system (a) and NBI system with bandpass filters of 415 ± 15 nm (b) and 540 ± 10 nm (c).

spectrum [e.g., the 415 nm narrow-band spectrum in 4(b)] by weighting OP values at each wavelength according to the relative spectral intensity. This made it possible to obtain a result using one set of weighted OPs and a single MC simulation. Table 1 shows weighted OPs for 415 ± 15 and 540 ± 10 nm bands and for white light (400–650 nm). The anisotropy factors (g) used for epithelium, mucosa, and blood were 0.95, 0.89, and 0.9, respectively.

A more rigorous yet time-consuming multi-wavelength approach was also evaluated. This approach involved performing 51 MC simulations per spectrum—one every 5 nm increment. The 2D spatial reflectance distributions for all increments were then weighted by spectral illumination intensity to determine the final reflectance image. Comparisons of single- and multiple-simulation approach results were performed to identify cases for which a single-simulation approach was valid and thus could be used to simplify the modeling process.

Table 1. Weighted OPs (in cm^{-1}) for 415 and 540 nm Bands and White Light

	Epithelium		Mucosa		Blood	
Wavelength	μ_a	μ_s	μ_a	μ_s	μ_a	μ_s
415 ± 15 nm	3.0	105.4	26.2	287	2380.9	1241
540 ± 10 nm	1.8	80.5	4.4	210	274.4	337
White light	1.9	84	5.5	220.9	356.6	406

D. Experimental Validation

As validation of the simulated contrast results, experimental measurements were performed using a fiberoptic-coupled Xenon light source (HPX-2000, Ocean Optics, Dunedin, Florida), band-pass filters (415 ± 15 nm and 540 ± 10 nm, Newport Corporation, Irvine, California), and a CCD camera (U2000, Apogee Imaging Systems, Roseville, California) with a macro zoom lens (18–108 mm, Edmund Optics Inc., Barrington, New Jersey). The distance from the lens to the sample was 15 cm and the diameter of the lens was 4.5 cm. Single-layer liquid phantoms were constructed with deionized water, ferrous stabilized Hb powder (Sigma-Aldrich, St. Louis, Missouri), and polystyrene microspheres (1.0 μm diameter, Polysciences Inc., Warrington, Pennsylvania). Phantom OPs were measured using a spectrophotometer (Shimadzu Inc., Columbia, Maryland) to ensure that samples had biologically accurate absorption levels. In order to achieve target OP values based on the literature (Fig. 1), microsphere concentrations were calculated with Mie theory. The phantom consisted of microspheres (0.72%) and Hb (3.4 mg/mL) in deionized water. To approximate a discrete blood vessel, a Hb solution (300 mg/mL) with μ_a values similar to those used in our simulations was injected into a glass capillary tube with inner/outer diameters of 100/120 μm and immersed in the liquid phantom. The range of capillary depths was limited due to the difficulty in producing liquid

Table 2. Comparison of Contrast Values for Single- and Multi-Simulation Approaches

Vessel Diameter (μm)		50					100				
Vessel Depth (μm)		25	75	125	175	225	50	150	250	350	450
415 ± 15 nm band	Single-	0.94	0.71	0.42	0.24	0.14	0.90	0.46	0.18	0.07	0.03
	Multi-	0.94	0.72	0.42	0.24	0.14	0.90	0.46	0.18	0.07	0.03
	Error (%)	0.1	0.4	0.7	0.9	3.2	0.2	0.2	2.2	2.1	18.8
540 ± 10 nm band	Single-	0.66	0.52	0.34	0.22	0.14	0.86	0.54	0.27	0.14	0.06
	Multi-	0.65	0.52	0.35	0.22	0.14	0.86	0.54	0.27	0.13	0.06
	Error (%)	0.3	0.1	2.4	0.4	0.2	0.1	1.0	1.0	2.0	0.2
400–650 nm	Single-	0.74	0.58	0.38	0.24	0.16	0.89	0.54	0.26	0.12	0.06
	Multi-	0.41	0.33	0.21	0.13	0.09	0.58	0.34	0.17	0.08	0.04
	Error (%)	79.0	78.8	80.6	79.4	85.5	52.9	55.9	58.5	58.4	55.1

layer thicknesses of less than 200 μm above the capillary tube. Figure 2 shows an optical coherence tomography (OCT) image of the vessel (capillary tube filled with Hb solution) at $Z_V = 300$ μm embedded in a liquid phantom. This visual representation demonstrates how the thickness of the phantom above the capillary tube was determined in experimental measurements. Each *en face* reflection image in the experimental measurement is made of approximately 200 × 200 pixels (~10 mm × 10 mm). Contrast values were then determined from rows of pixels in the same manner described for the simulation data.

3. Results and Discussion

A. Evaluation of Single-Simulation Method

Table 2 compares contrast values determined with the single-simulation method with those from the multi-simulation method. Results are presented for NBI bands of 415 and 540 nm and white light of 400–650 nm for vessel diameters of 50 and 400 μm. As shown in the table, 12 out of 16 cases for the 415 and 540 nm bands had a contrast difference of no more than 1% between the single- and multi-simulation methods. The remaining cases showed absolute discrepancies of less than 0.02, thus indicating that the single-simulation method was accurate for calculating the contrast for the 415 and 540 nm bands. However, the difference between single- and multi-simulations ranged from 33% to 98% when white light was used, indicating that the single-simulation method did not accurately model broadband light propagation. Therefore, all subsequent data provided for NBI simulations are based on the single-simulation method whereas those for white light are from the multi-simulation method (simulations every 5 nm from 400 to 650 nm).

B. Effect of Vessel Diameter and Depth

Simulated reflectance distributions are presented for a vessel size of 50 μm at four different depths ($Z_V = 20$, 100, 200, and 300 μm) based on 415 nm, 540 nm, and white light illumination (Fig. 5). In these images, contrast decreased strongly with Z_V. For the 20 μm depth case, the 415 nm band appeared to produce slightly higher contrast than the 540 nm band while white light produced lowest contrast. At deeper regions ($Z_V = 200$ and 300 μm), the 540 nm band produced highest contrast followed by 415 nm and white light.

Fluence distributions at 415 and 540 nm are presented in Fig. 6 to further illustrate the effect of wavelength and vessel geometry on light propagation. For all cases, there is a strong reduction in fluence within the vessel as well as a shadowing effect below the vessel. These effects are stronger at 415 nm than 540 nm due to the higher μ_a and the reduction in fluence at the superficial edge of vessels is sharper at 415 nm. As vessel depth increases, shadows appear to become shorter and more diffuse. These graphs also illustrate reduced penetration depth throughout the tissue region at 415 nm relative to 540 nm. Fluence decays to very low levels by 300 μm below the surface for 415 nm, whereas the decay in fluence with depth is less than half as strong at 540 nm.

In order to better illustrate the light propagation processes that induce contrast in detected images, we also generated fluence distributions based only on photons that were remitted within the designated aperture—the same photons that made up the imaged reflectance distributions [e.g., in Fig. 3(a)]. The most notable feature in the detected-photon fluence results (Fig. 7) is a bi-directional vessel shadowing effect, as opposed to the shadows below the

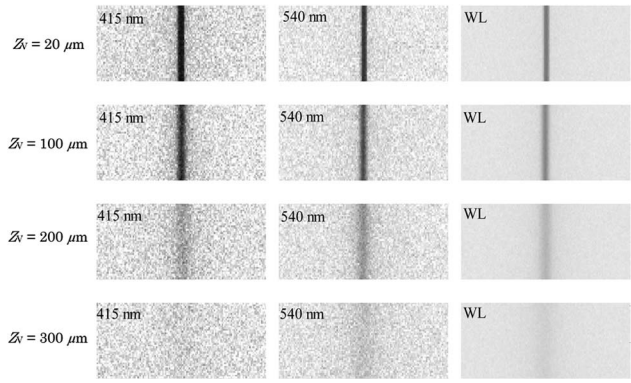

Fig. 5. Simulated reflectance distributions for 415 nm, 540 nm, and white light illumination of tissue for Z_V values of 20–300 μm and $D = 50$ μm. Each image represents an area of 0.4 × 1.4 mm (height × width).

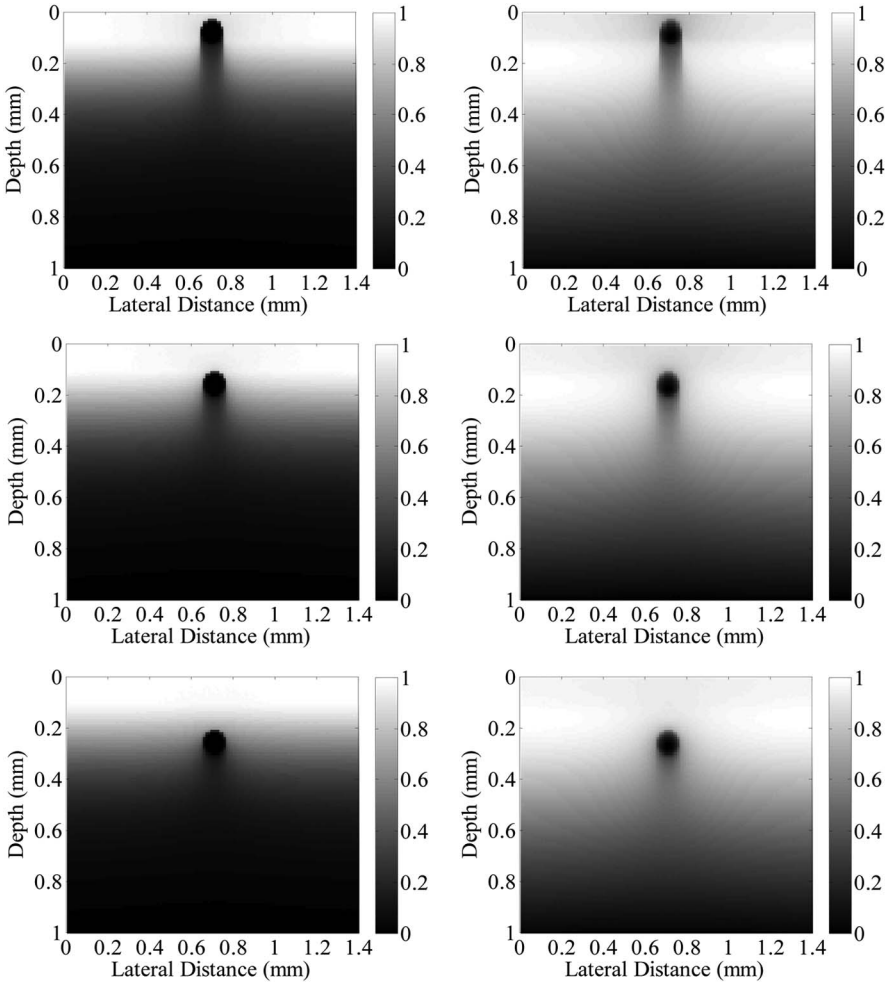

Fig. 6. Fluence distributions for 415 and 540 nm illumination (left and right columns, respectively), where $Z_V = 20$, 100, and 200 μm (top to bottom) and $D = 100$ μm.

vessels seen in standard fluence distributions. This is likely due to the fact that photons traveling in a ballistic manner toward the surface are preferentially detected within the restricted cone angle. In the presence of a vessel, photons that would otherwise have propagated toward the surface and been detected, are absorbed. As vessel depth increases, there is a greater chance that photons that did not interact with the vessel region can be scattered into trajectories within the cone angle, thus "filling in" the shadow and reducing vessel contrast. These results show that the effect of vessel shading decreases more rapidly with depth for 415 nm than 540 nm illumination in a manner analogous to the contrast results for the $D = 100$ μm case in Fig. 8(c).

Vessel contrast as a function of Z_V and D for 415 and 540 nm bands as well as white light are presented in Fig. 8. In general, as Z_V increased, contrast decreased because photon penetration depth was limited by scattering and absorption in tissue above the vessel. The rate of this decrease was dependent on vessel size and wavelength, with small vessels at 415 nm decreasing most rapidly with depth and large vessels at 540 nm decreasing the slowest. These graphs provide quantitative characterization of the improvement provided by NBI over broadband white light imaging. White light illumination does not provide higher contrast than both NBI cases for any vessel geometry. The 415 nm band produced greater contrast than white light for smaller and shallower vessels (up to 300%) but slightly less contrast for larger and deeper vessels. This was likely because the longer wavelength region of the white light was less scattered and less absorbed than 415 nm light and could penetrate deeper, producing higher contrast. Imaging at 540 nm always produced greater contrast (up to 93%) than white light due to the higher vessel absorption on average.

Results in Fig. 8 also provide quantitative predictions of differences in contrast between 415 and 540 nm. For small vessels at superficial depths ($20\ \mu\text{m} \le D \le 50\ \mu\text{m}$, $20\ \mu\text{m} \le Z_V \le 200\ \mu\text{m}$), the 415 nm band produced higher contrast (up to 125%) than the 540 nm band [Figs. 8(a) and 8(b)]. This was because Hb absorption is a factor of 8.7 greater at 415 nm than 540 nm (2381 cm^{-1} versus 274 cm^{-1}). As a result, the fraction of light that can penetrate the width of a small vessel is much lower at 415 nm than 540 nm. This discrepancy in maximum contrast decreases with vessel diameter, with superficial

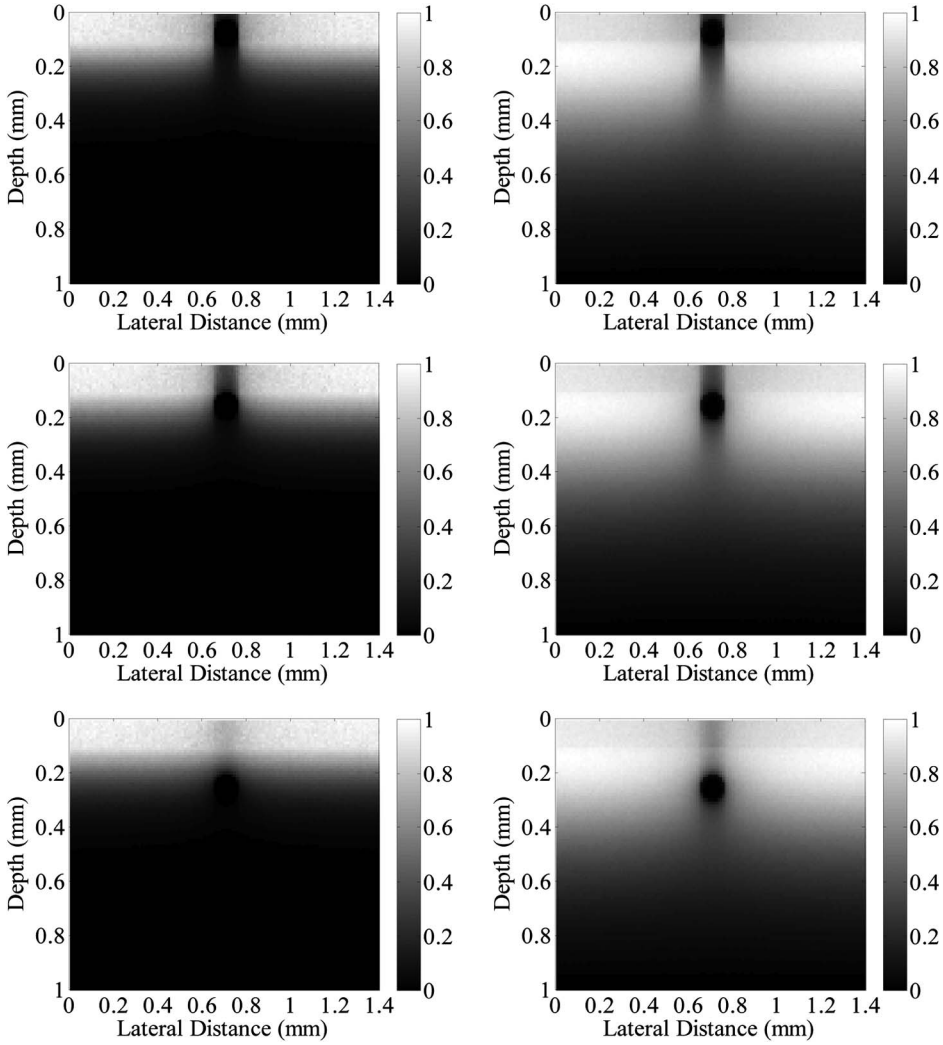

Fig. 7. Detected-photon fluence distributions for 415 and 540 nm illumination (left and right columns, respectively), where $Z_V = 20100$, and 200 μm (top to bottom) and $D = 100$ μm.

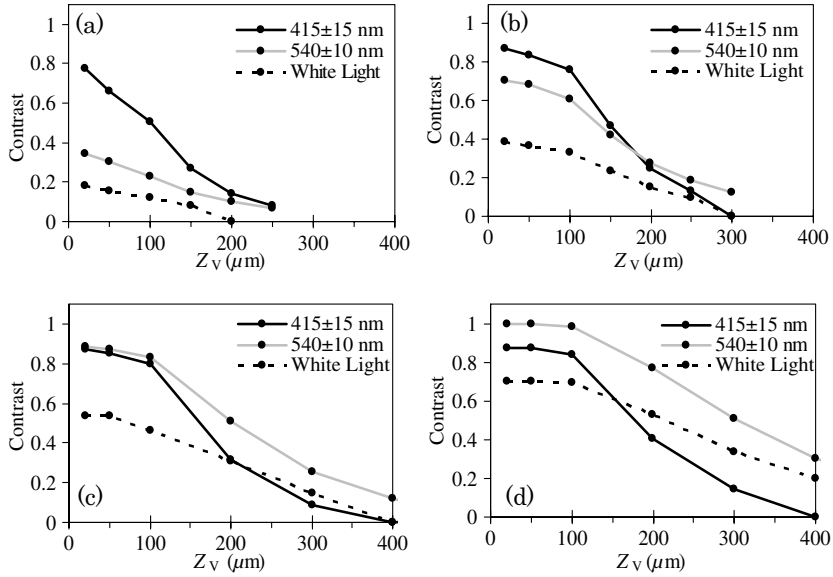

Fig. 8. Contrast as function of vessel depth (Z_V) for diameters (D) of (a) 20 μm, (b) 50 μm, (c) 100 μm, and (d) 400 μm for 415 nm, 540 nm, and white light illumination.

100 μm diameter vessels showing nearly equivalent contrast at both wavelengths [Fig. 8(c)]. For larger vessels in deeper regions (100 μm $\leq D \leq$ 400 μm, 150 μm $\leq Z_V \leq$ 400 μm), 540 nm produced higher contrast (up to 250%) than 415 nm [Figs. 8(c) and 8(d)]. This was because bulk tissue attenuation at 540 nm is lower than at 415 nm, mostly due to absorption, as indicated in our prior study [25]. In addition, for any given vessel depth, vessel diameter had less effect on contrast at 415 nm than at 540 nm or for white light due to the dominant absorption at 415 nm discussed above. Even short photon path lengths through narrow vessels cause nearly complete absorption at 415 nm, whereas for 540 nm and white light an increase in vessel diameter increases the probability of a photon being absorbed by hemoglobin.

C. Effect of Wavelength

In order to elucidate the influence of spectral variations in illumination on image contrast, we performed simulations over the 400–650 nm range (Fig. 9). These results provide a comprehensive illustration of the effect of vessel diameter and depth as well as wavelength and reveal an apparent contradiction—that the Hb absorption band at 415 nm can both improve and degrade vascular contrast. While high absorption due to intravascular Hb can increase contrast, the widespread decrease in fluence due to bulk absorption in vascular tissue may reduce contrast at a specific vessel of interest. These competing effects result in the contrast curves in Fig. 9 varying in direct proportional to Hb μ_a at most wavelengths, except at 415 nm, where there is an inverse relationship. Therefore, in spite of the fact that 415 nm provides superior contrast for the most superficial vessels, 445 nm light may provide better contrast for larger/deeper vasculature [9,10]. Another key effect seen in Fig. 9 is the decreasing significance of Hb μ_a on spectral variations in contrast as vessel depth increases. The contrast curves for these vessels are largely flat, with a slight positive slope. This indicates a transition from absorption-dominated contrast and toward increased dependence on tissue scattering, with the positive slope due to decreasing scattering (and increased penetration) with wavelength. The one significant effect of Hb μ_a for deep vessels is the trough in contrast at the Soret band. Therefore, the finding in our prior study that the difference in contrast between 415 and 540 nm for larger, deeper vessels is primarily due to absorption rather than scattering [25] represents an exception to the general rule that contrast in these vessels is scattering-dominated, which applies to wavelengths from 450 to 600 nm.

D. Comparison with Experimental Results

In order to validate the numerical model, we compared results with our experimental measurements as well as *in vivo* data from the literature. Images of the capillary tube-based phantom imaged under 415 nm, 540 nm, and white light illumination are presented in Fig. 10. A quantitative comparison of experimentally determined contrast values with simulations is shown in Fig. 11. Good agreement was seen at $Z_V = 300$ and 400 μm, as experimental results were within 18% of simulations for nonzero contrast values. However, experimental results were only within 42% of simulations at $Z_V = 200$ μm. Discrepancies were likely due to factors such as the 20 μm capillary tube wall thickness, nonuniformity in illumination, and errors in capillary tube depth

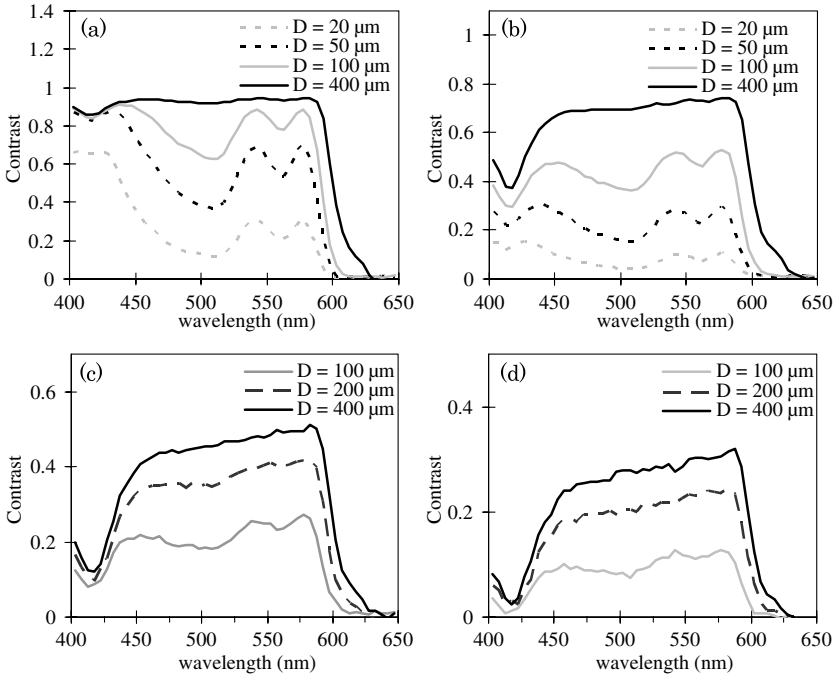

Fig. 9. Contrast as a function of wavelength for different vessel diameters when Z_V is (a) 50 μm, (b) 200 μm, (c) 300 μm, and (d) 400 μm.

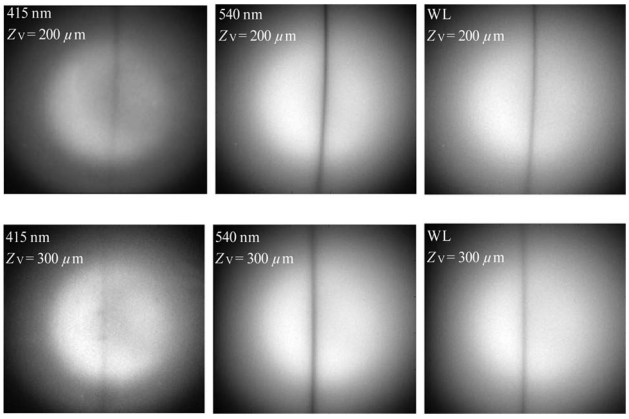

Fig. 10. Experimental images of capillary tube phantom ($D = 100$ μm) under 415 nm, 540 nm, and white light (WL) illumination for $Z_V = 200$ μm and $Z_V = 300$ μm.

positioning. The high level of discrepancy for 200 μm vessel depths was likely due to difficulty in obtaining a constant level of liquid above the capillary tube, due to surface tension. Although we attempted to mitigate layer thickness uncertainty by validating depth through OCT imaging—which indicated that depths were typically within 10% of expected values—it was not possible to collect OCT and NBI images with the phantom on the same platform.

Further evidence of the validity of our modeling results can be obtained through comparisons with data from the literature (Table 3). However, in spite of the numerous *in vivo* NBI studies that have been published, few provide measured data on the size and depth of imaged vessels or quantitative results on vessel contrast. Early studies by Gono *et al.* [13] included *in vivo* data on contrast; however, these results did not specify the depth of imaged vessels. For vessels termed "class 1" ($D = 20$ μm), they found mean contrast levels at 415 ± 15 and 540 ± 10 nm of 0.38 ± 0.1 and 0.24 ± 0.1, respectively. Our simulations predicted contrast levels for $D = 20$ μm and $Z_V = 20$–150 μm ranging from 0.78 to 0.27 for 415 nm and from 0.35 to 0.15 for 540 nm. By interpolating this data [Fig. 8(a)], it was found that

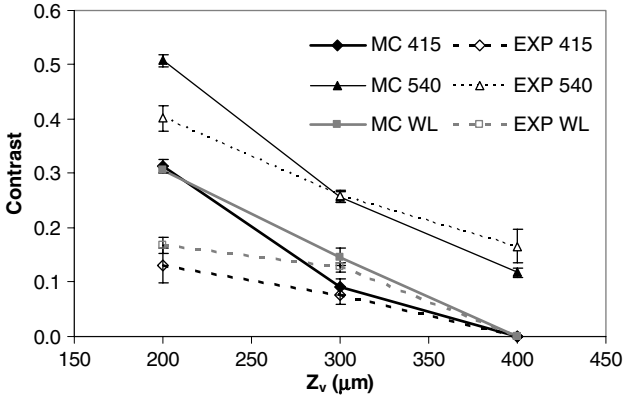

Fig. 11. Quantitative contrast results for three capillary tube depths (Z_V) in Monte Carlo simulations (MC) and experimental measurements (EXP).

values for $Z_V = 125$ μm (0.39 and 0.19, for 415 and 540 nm, respectively) most closely matched the results from Gono *et al.* Experimental data on larger vessels were measured by Akbari *et al.* during porcine laparoscopic surgery [23]. While the size and depth of the porcine arteries imaged in this study were not determined, contrast values for white light and NBI at 540 nm were reported as 0.17 ± 0.06 and 0.35 ± 0.06. These values are in moderately good agreement with those seen in our results for large, deep vessels [Figs. 8(c) and 8(d)]—low contrast for white light and slightly higher contrast for 540 nm illumination. In spite of the lack of data on tissue morphology in these prior *in vivo* studies, our results appear to be in good general agreement with their findings.

E. Alternate NBI Wavelengths

Our results support the potential utility of NBI wavelengths such as 445, 500, and 575 nm that have been noted in the literature [6,38]. Figure 9 shows that for small, superficial vessels, higher contrast was produced at 415 nm than 540 nm and 575 nm. However, for depths of 50 μm or more, contrast at 445 nm was similar to or greater than that at 415 nm. This agrees with results from Gono *et al.* indicating that 415 nm illumination produces 42% higher contrast than 445 nm for superficial small vessels ($D \leq 20$ μm) while 445 nm produces approximately 12% higher contrast than 415 nm for larger vessels (20 μm $\leq D \leq 50$ μm) at deeper regions. Our results also indicate that 575 nm produces greater contrast than 415, 445, or 540 nm illumination [Fig. 9(b)] for large vessels ($D \geq 100$ μm) at deep regions, likely due to spectral variations in tissue scattering. The slightly higher contrast at 575 nm relative to the more standard 540 nm band indicates the potential utility of the former wavelength, particularly for larger, deeper vessels [38]. However, the proximity of this absorption peak at 575 nm to a strong drop off in Hb μ_a near 600 nm may indicate that a narrow bandpass would be required for this wavelength to be effective.

F. Limitations

The results of our simulations and phantom measurements indicate that the true underlying mechanisms of NBI may not be as well understood as studies in the literature suggest. Results indicate that scattering is not sufficiently different across wavelengths to induce significant variations in contrast. Our results indicate that mucosal absorption likely plays a key role in attenuating light within mucosa, due to the very strong variations in Hb absorption, particularly in the Soret band near 405 nm. However, our model ignores several key factors that may influence NBI contrast. First, Hb is not uniformly distributed in tissue. Thus, local levels of attenuation due to absorption may vary significantly, creating regions of high attenuation where vasculature is dense and regions of low attenuation and

Table 3. Comparison of Simulated NBI Contrast Values with Prior *in vivo* Studies

	Prior *In vivo* Study Results		NBI Simulations	
	Akbari *et al.* [23]	Gono *et al.* [13]		
Vessel size	N/A (porcine artery)	10–20 μm (human tongue)	100 μm	20 μm
Vessel depth	N/A	N/A	250 μm	125 μm
Contrast: white light	0.17 ± 0.06	N/A	0.23 ± 0.00	0.10 ± 0.00
Contrast: 415 ± 10 nm	N/A	0.38 ± 0.05	0.17 ± 0.01	0.39 ± 0.00
Contrast: 540 ± 10 nm	0.35 ± 0.06	0.24 ± 0.05	0.36 ± 0.00	0.19 ± 0.00

higher contrast where vasculature is sparse. Given the wide variations in vascular patterns seen in mucosal tissues, the actual contrast achieved, and its variation with depth, may vary significantly from the levels estimated in the current study. However, we have performed limited simulations incorporating discrete network of cylindrical vessels in a background Hb-free mucosa region, and found good agreement with our current results.

Finally, it should also be noted that this study focuses on grayscale contrast values and does not take into account the color representation often incorporated into commercial endoscopic devices. This approach is similar to that taken in prior studies by Gono *et al.* [13,14], and while it provides useful quantitative insight into the fundamental light-tissue interactions involved in spectral imaging of vasculature, it represents an idealized imaging scenario that may not provide a direct correlation with results from clinical devices.

4. Conclusions

In this study, we have used numerical modeling and experimental measurements of tissue phantoms to elucidate the effect of wavelength and vessel geometry on contrast in narrow-band and white light imaging of mucosal vasculature. Our modeling results provide quantitative characterization of how spectral variations in absorption and scattering, as well as vessel morphology, influence contrast. Specifically, the transition from superior contrast at 415 to 540 nm with increased vessel depth and diameter was illustrated, and the level of improvement provided by NBI over white light imaging was shown to range from 35% to 300%. This work also indicated that under certain conditions, other wavelengths such as 445 nm may be equally or more effective than 415 or 540 nm illumination. Phantom measurements provided validation of numerical results, yet also indicated that the development of new physical models to study light propagation in tissue with small, superficial blood vessels would be beneficial. While computationally intensive, the Monte Carlo approach presented in this study was highly flexible and useful for studying a variety of scenarios and effects that provided quantitative insights into NBI and may lead to improved device designs. In the future, it may also be possible to apply some of the methods and concepts developed in this study to optimize NBI-based approaches for imaging contrast agents and nanoparticles.

The authors would like to thank professor Ian White of the University of Maryland, College Park for fabrication of the capillary tubes used in this study. The mention of commercial products, their sources, or their use in connection with material reported herein is not to be construed as either an actual or implied endorsement of such products by the Department of Health and Human Services.

References

1. R. Siegel, E. Ward, O. Brawley, and A. Jemal, "Cancer statistics, 2011," Ca—Cancer J. Clin. **61**, 212–236 (2011).
2. Y. Kumagai, M. Toi, and H. Inoue, "Dynamism of tumour vasculature in the early phase of cancer progression: outcomes from oesophageal cancer research," Lancet Oncol. **3**, 604–610 (2002).
3. C. Torres, H. Wang, J. Turner, A. Shahsafaei, and R. D. Odze, "Prognostic significance and effect of chemoradiotherapy on microvessel density (angiogenesis) in esophageal Barrett's esophagus-associated adenocarcinoma and squamous cell carcinoma," Human Pathology **30**, 753–758 (1999).
4. M. Auvinen, E. Sihvo, T. Ruohtula, J. T. Salminen, A. Koivistoinen, P. Siivola, R. Rönnholm, J. O. Rämö, M. Bergman, and J. A. Salo, "Incipient angiogenesis in Barrett's epithelium and lymphangiogenesis in Barrett's adenocarcinoma," J. Clin. Oncol. **20**, 2971–2979 (2002).
5. H. M. Chiu, C. Chang, C. Chen, Y. Lee, M. Wu, J. Lin, C. Shun, and H. Wang, "A prospective comparative study of narrow-band imaging, chromoendoscopy, and conventional colonoscopy in the diagnosis of colorectal neoplasia," Gut **56**, 373–379 (2007).
6. M. Y. Su, C. Hsu, Y. Ho, P. Chen, C. Lin, and C. Chi, "Comparative study of conventional colonoscopy, chromoendoscopy, and narrow-band imaging systems in differential diagnosis of neoplastic and nonneoplastic colonic polyps," Am. J. Gastroenterol. **101**, 2711–2716 (2006).
7. Y. Hamamoto, T. Endo, K. Nosho, Y. Arimura, M. Sato, and K. Imai, "Usefulness of narrow-band imaging endoscopy for diagnosis of Barrett's esophagus," J. Gastroenterol. **39**, 14–20 (2004).
8. P. Sharma, A. Bansal, S. Mathur, S. Wani, R. Cherian, D. McGregor, A. Higbee, S. Hall, and A. Weston, "The utility of a novel narrow band imaging endoscopy system in patients with Barrett's esophagus," Gastrointest. Endosc. **64**, 167–175 (2006).
9. J. H. Takano, T. Yakushiji, I. Kamiyama, T. Nomura, A. Katakura, N. Takano, and T. Shibahara, "Detecting early oral cancer: narrowband imaging system observation of the oral mucosa microvasculature," Int. J. Oral Maxillofac. Surg. **39**, 208–213 (2010).
10. T. Yoshida, H. Inoue, S. Usui, H. Satodate, N. Fukami, and S. Kudo, "Narrow-band imaging system with magnifying endoscopy for superficial esophageal lesions," Gastroint. Endosc. **59**, 288–295 (2004).
11. P. Sharma, S. Wani, A. Bansal, S. Hall, S. Puli, S. Mathur, and A. Rastogi, "A feasibility trial of narrow band imaging endoscopy in patients with gastroesophageal reflux disease," Gastroenterology **133**, 454–464 (2007).
12. W. L. Curvers, C. J. Bohmer, R. C. Mallant-Hent, A. H. Naber, C. I. J. Ponsioen, K. Ragunath, R. Singh, M. B. Wallace, H. C.

Wolfsen, L.-M. Wong Kee Song, R. Lindeboom, P. Fockens, and J. J. Bergman, "Mucosal morphology in Barrett's esophagus: interobserver agreement and role of narrow band imaging," Endoscopy **40**, 799–805 (2008).
13. K. Gono, T. Obi, M. Yamaguchi, N. Ohyama, H. Machida, Y. Sano, S. Yoshida, Y. Hamamoto, and T. Endo, "Appearance of enhanced tissue features in narrow-band endoscopic imaging," J. Biomed. Opt. **9**, 568–577 (2004).
14. K. Gono, K. Yamazaki, N. Doguchi, T. Nonami, T. Obi, M. Yamaguchi, N. Ohyama, H. Machida, Y. Sano, Y. Yoshida, Y. Hamamoto, and T. Endo, "Endoscopic observation of tissue by narrow band illumination," Opt. Rev. **10**, 211–215 (2003).
15. T. Itoi, A. Sofuni, F. Itokawa, T. Tsuchiya, T. Kurihara, K. Ishii, S. Tsuji, F. Moriyasu, and T. Gotoda, "Peroral cholangioscopic diagnosis of biliary-tract diseases by using narrow-band imaging (with videos)," Gastrointest. Endosc. **66**, 730–736 (2007).
16. K. Nonaka, M. Namoto, H. Kitada, M. Shimizu, Y. Ochiai, O. Togawa, M. Nakao, M. Nishimura, K. Ishikawa, S. Arai, and H. Kita, "Usefulness of the DL in ME with NBI for determining the expanded area of early-stage differentiated gastric carcinoma," World J. Gastrointest. Endosc. **4**, 362–367 (2012).
17. F. J. F. Herth, R. Eberhardt, D. Anantham, D. Gompelmann, M. W. Zakaria, and A. Ernst, "Narrow-band imaging bronchoscopy increases the specificity of bronchoscopic early lung cancer detection," J. Thorac. Oncol. **4**, 1060–1065 (2009).
18. M. J. Waldner, S. Wirtz, C. Neufert, C. Becker, and M. F. Neurath, "Confocal laser endomicroscopy and narrow-band imaging-aided endoscopy for in vivo imaging of colitis and colon cancer in mice," Nat. Protoc. **6**, 1471–1481 (2011).
19. T. Fujii, M. Nakamura, K. Kameyama, M. Saito, H. Nishio, A. Ohno, N. Hirao, T. Iwata, K. Tsukazaki, and D. Aoki, "Digital colposcopy for the diagnosis of cervical adenocarcinoma using a narrow band imaging system," Int. J. Gynecol. Cancer **20**, 605–610 (2010).
20. American College of Obstetricians and Gynecologists, "ACOG Practice Bulletin number 99 Management of abnormal cervical cytology and histology," Obstet. Gynecol. **112**, 1419–1444 (2008).
21. J. E. Frank, "The colposcopic examination," J Midwifery Womens Health **53**, 447–452 (2008).
22. B. S. Apgar, M. M. Rubin, and G. L. Brotzman, "Principles and techniques of the colposcopic examination," in *Colposcopy Principles and Practice: An Integrated Textbook and Atlas*, B. S. Apgar, ed. (WB Saunders, 2002).
23. H. Akbari, Y. Kosugi, K. Kojima, T. Ohya, H. Akamatsu, and N. Tanaka, "Enhanced blood vessels in laparoscopy by using narrow-band imaging," in *Proceedings of the 10th IAPR Conference on Machine Vision Applications* (IAPR, 2007), pp. 244–247.
24. American Society of Gastrointestinal Endoscopy, "Narrow band imaging and multiband imaging," Gastrointest. Endosc. **67**, 581–589 (2008).
25. D. V. N. Le, Q. Wang, J. C. Ramella-Roman, and T. J. Pfefer, "Monte Carlo modeling of light–tissue interactions in narrow band imaging," J. Biomed. Opt. **18**, 010504 (2013).
26. T. J. Pfefer, J. K. Barton, E. K. Chan, M. G. Ducros, B. S. Sorg, T. E. Milner, J. S. Nelson, and A. J. Welch, "A three-dimensional modular adaptable grid numerical model for light propagation during laser irradiation of skin tissue," IEEE J. Sel. Top. Quantum Electron. **2**, 934–942 (1996).
27. G. W. Lucassen, W. Verkruysse, M. Keijzer, and M. J. C. van Gemert, "Light distributions in a port wine stain model containing multiple cylindrical and curved blood vessels," Lasers Surg. Med. **18**, 345–357 (1996).
28. Y. Chen, A. D. Aguirre, P.-L. Hsiung, S. Desai, P. R. Herz, M. Pedrosa, Q. Huang, M. Figueiredo, S. W. Huang, A. Koski, J. M. Schmitt, J. G. Fujimoto, and H. Mashimo, "Ultrahigh resolution optical coherence tomography of Barrett's esophagus: preliminary descriptive clinical study correlating images with histology," Endoscopy **39**, 599–605 (2007).
29. D. C. Walker, B. H. Brown, A. D. Blackett, J. Tidy, and R. H. Smallwood, "A study of the morphological parameters of cervical squamous epithelium," Physiol. Meas. **24**, 121–135 (2003).
30. M. H. Johnston, "Technology insight: ablative techniques for Barrett's esophagus—current and emerging trends," Nature Clin. Prac. Gastro. Hepat. **2**, 323–330 (2005).
31. D. O. Faigel, D. A. Lieberman, W. M. Weinstein, S. Fanning, M. B. Fennerty, and R. B. Sampliner, "Effect of multipolar electrocoagulation and EUS findings in Barrett's esophagus," Gastrointest. Endosc. **55**, 23–26 (2002).
32. R. Drezek, K. Sokolov, U. Utzinger, I. Boiko, A. Malpica, M. Follen, and R. Richards-Kortum, "Understanding the contributions of NADH and collagen to cervical tissue fluorescence spectra: modeling, measurements, and implications," J. Biomed. Opt. **6**, 385–396 (2001).
33. J. Qu, C. MacAulay, S. Lam, and B. Palcic, "Optical properties of normal and carcinomatous bronchial tissue," Appl. Opt. **33**, 7397–7405 (1994).
34. M. Friebel, A. Roggan, G. Müller, and M. Meinke, "Determination of optical properties of human blood in the spectral range 250 to 1100 nm using Monte Carlo simulations with hematocrit-dependent effective scattering phase function," J. Biomed. Opt. **11**, 034021 (2006).
35. P. Puvanakrishnan, J. Park, P. Diagaradjane, J. A. Schwartz, C. L. Coleman, K. L. Gill-Sharp, K. L. Sang, J. D. Payne, S. Krishnan, and J. W. Tunnel, "Near-infrared narrow-band imaging of gold/silica nanoshells in tumors," J. Biomed. Opt. **14**, 024044 (2009).
36. K. Kuznetsov, R. Lambert, and J.-F. Rey, "Narrow-band imaging: potential and limitations," Endoscopy **38**, 76–81 (2006).
37. H. Mizuno, Y. Sano, Y. Hamamoto, M. Muto, T. Kozu, H. Tajiri, and S. Yoshida, "Narrow band imaging technique," Tech. Gastroin. Endosc. **5**, 78–81 (2003).
38. D. Roblyer, C. Kurachi, V. Stepanek, R. A. Schwarz, M. D. Williams, A. K. El-Naggar, J. J. Lee, A. M. Gillenwater, and R. Richards-Kortum, "Comparison of multispectral wide-field optical imaging modalities to maximize image contrast for objective discrimination of oral neoplasia," J. Biomed. Opt. **15**, 066017 (2010).